RESEARCH ARTICLE

Key Points:
- Ion flux in trapped ring current during main phase of large storm shows multiple peaks
- Pressure anisotropy tends toward parallel at large radii
- The TWINS ion images are compared directly with RBSPICE-A in situ measurements

Correspondence to:
J. D. Perez,
perez@physics.auburn.edu

Global images of trapped ring current ions during main phase of 17 March 2015 geomagnetic storm as observed by TWINS

J. D. Perez[1], J. Goldstein[2,3], D. J. McComas[2,3], P. Valek[2,3], M.-C. Fok[4], and Kyoung-Joo Hwang[4,5]

[1]Physics Department, Auburn University, Auburn, Alabama, USA, [2]Southwest Research Institute, San Antonio, Texas, USA, [3]Department of Physics, University of Texas at San Antonio, San Antonio, Texas, USA, [4]NASA Goddard Space Flight Center, Greenest, Maryland, USA, [5]The Goddard Planetary and Heliophysics Institute, University of Maryland, Baltimore County, Baltimore, Maryland, USA

Abstract A unique view of the trapped particles in the inner magnetosphere provided by energetic neutral atom (ENA) imaging is used to observe the dynamics of the spatial structure and the pitch angle anisotropy on a global scale during the last 6 h of the main phase of a large geomagnetic storm (minimum $SYM\text{-}H = -230$ nT) that began on 17 March 2015. Ion flux and pressure anisotropy obtained from Two Wide-angle Imaging Neutral-atom Spectrometers (TWINS) ENA images are shown. The ion flux shows two peaks, an inner one at approximately radii = 3–4 R_E in the dusk-to-midnight sector and an outer peak at radii = 8–9 R_E prior to midnight. The inner peak is relatively stationary during the entire period with some intensification during the final steep decline in $SYM\text{-}H$ to its minimum. The outer peak shows the significant temporal variation brightening and dimming and finally disappearing at the end of the main phase. The pressure anisotropy shows the expected perpendicular pitch angles inside of $L = 6$ but shows parallel pitch angles at greater L values. This is interpreted as consistent with pitch angle-dependent drift as modeled in the Tsy05 magnetic field and Comprehensive Inner Magnetosphere-Ionosphere simulations. The TWINS results are compared directly with Radiation Belt Storm Probes Ion Composition Experiment (RBSPICE)-A measurements. Using 15 min snapshots of flux and pressure anisotropy from TWINS along the path of RBSPICE-A during the 6 h focused upon in this study, the essential features displayed in the TWINS global images are supported.

1. Introduction

Observing the characteristics of particles injected from the magnetotail and trapped in the Earth's ring current is important for understanding the dynamics of the inner magnetosphere. While an extensive history of in situ measurements has made significant contributions to progress in this area, there is still much to be learned. In this study, we take advantage of a unique view of the trapped particles in the inner magnetosphere provided by energetic neutral atom (ENA) imaging to observe the dynamics of the spatial structure and the pitch angle anisotropy on a global scale. We focus on the last 6 h of the main phase of a large geomagnetic storm that began on 17 March 2015. From ENA images obtained by Two Wide-angle Imaging Neutral-atom Spectrometers (TWINS) [*McComas et al.*, 2009a; *Goldstein and McComas*, 2013], we extract ion distribution images that show global time-dependent spatial structure with multiple peaks and pitch angle anisotropy with both perpendicular and parallel regions. The pitch angle features of the observations are discussed in terms of drift in a nondipole magnetic field configuration. Simulation results from the Comprehensive Inner Magnetosphere-Ionosphere (CIMI) model [*Fok et al.*, 2014] show that the observations are consistent with expected drift motion under the conditions given by the Tsy05 [*Tsyganenko and Sitnov*, 2005] model field. In situ measurements by the Radiation Belt Storm Probes Ion Composition Experiment (RBSPICE) [*Mitchell et al.*, 2013] aboard the Van Allen Probes (formerly known as the Radiation Belt Storm Probes (RBSP) A and B) [*Mauk et al.*, 2013; *Spence et al.*, 2013] show features similar to those observed in the TWINS ENA images.

Section 2 of this paper describes the data sources and methodology for obtaining ion distributions from the ENA images and describes the sources of the in situ experimental data. Section 3 presents the observations. Section 4 discusses the science related to the observations. Section 5 addresses the questions of confidence in the results of this study. Section 6 summarizes and concludes.
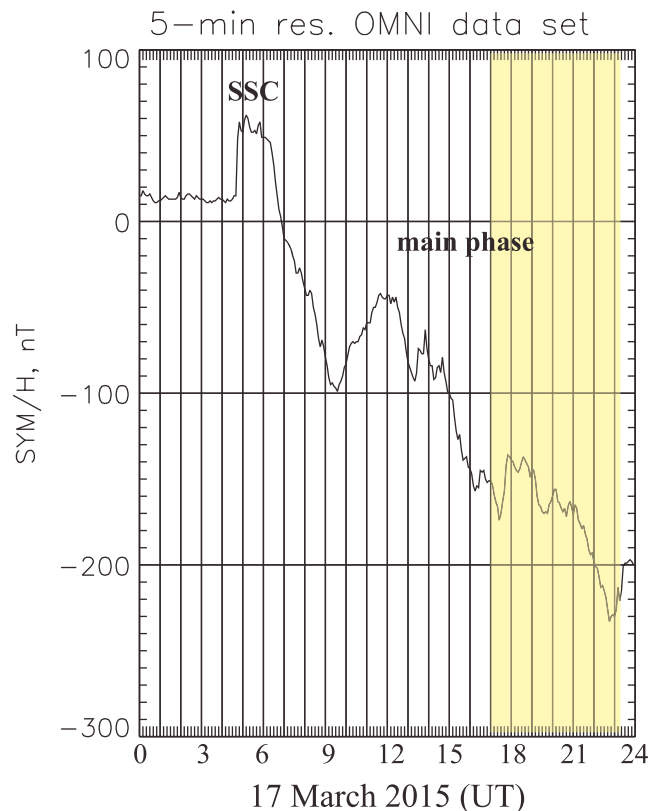
2. Data Sources and Analysis Methodology

The ENA images used in this study are from TWINS-1 of the NASA TWINS mission of opportunity [*McComas et al.*, 2009a; *Goldstein and McComas*, 2013]. Data from TWINS-2 are not available during this period. The instrument concept was initially described by *McComas et al.* [1998]. Full images are acquired every 72 s with an integration (sweep) time of 60 s. The images used in this study are integrated over 15–16 sweeps corresponding to ≈15 min of observation time during an ≈20 min time period. Neutral atoms are detected with energies from 1 to 100 keV/amu and scanned in energy to produce an image with $\Delta E/E = 1.0$ for H atoms. The TWINS ENA images are processed using a statistical smoothing technique and background suppression algorithms described in detail in Appendix A of *McComas et al.* [2012]. The TWINS statistical smoothing is adapted from the technique that was successfully applied to data from IBEX [*McComas et al.*, 2009b].

Figure 1. *SYM-H* data for 17 March 2015 during the main phase of a large storm. Source is http://omniweb.gsfc.nasa.gov/form/omni_min.html.

Following *Perez et al.* [2012, Appendix A], this study examines two key quantities derived from TWINS ENA images: (1) ion equatorial flux integrated over pitch angles and (2) pressure anisotropy, both as a function of time and location. The ion equatorial pitch angle distribution is expanded in a linear combination of tricubic splines [*deBoor*, 1978]. Minimizing a combination of normalized chi-square and a penalty function derived by *Wahba* [1990] allows the determination of the expansion coefficients. The penalty function ensures that the result is as smooth (in the sense of a minimum second derivative) as is consistent with fitting the data. Therefore, spatial structure is minimized and appears in the result only to the extent that it is statistically required to fit the data, i.e., match the ENA images. Thus, while finer spatial scale structure may also be present, the structure found represents the minimum that is statistically required by the data. The TWINS ENA images are integrated over energy bands with widths equal to the central energy; e.g., 30 keV images are integrated from 15 to 45 keV.

In order to obtain ion distributions from an ENA image a magnetic field model is required. In this study, the *Tsyganenko and Sitnov* [2005] model is used. ENA emissions contain two components. First, there are the high-altitude emissions (HAEs) that are due to charge exchange of the energetic ions with neutral hydrogen in the geocorona. These emissions are treated as coming from a thin target emitter. To treat the HAEs, a model of the density of the geocorona is needed. The TWINS exospheric neutral hydrogen density model [*Zoennchen et al.*, 2015] for solar maximum is used. Second, there are low-altitude emissions (LAEs) [*Roelof*, 1997] that are due to charge exchange of the energetic ions with neutral oxygen at altitudes below ≈600 km. These emissions are treated as originating from a thick target. The thick target approximation of *Bazell et al.* [2010] is used to quantify contributions from LAEs.

The in situ plasma data used in this study are obtained from the Van Allen Probes mission [*Mauk et al.*, 2013; *Spence et al.*, 2013]. In particular, we use the RBSPICE [*Mitchell et al.*, 2013] instrument, which is a time-of-flight
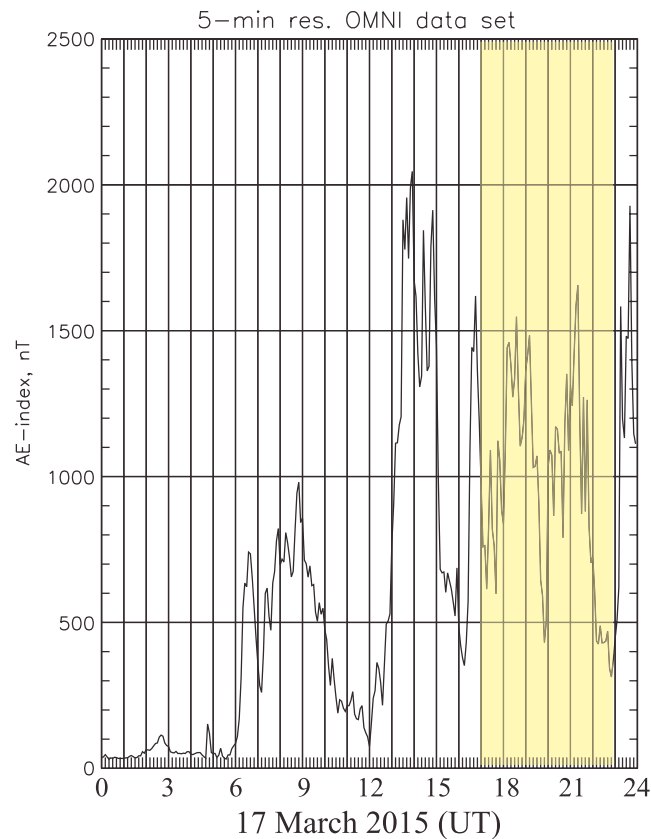
Figure 2. *AE* index for 17 March 2015 during the main phase of a large storm. Source is http://omniweb.gsfc.nasa.gov/form/omni_min.html.

mass spectrometer on satellite "A." The instrument records the energy and angle of medium energy protons, electrons, and ions (H^+, He^+, and O^+) sampling over a full 160° range of look directions in 3-D. In this study, the total proton flux at 30 keV and the ion pressure anisotropy obtained from http://rbspice.ftecs.com/Data.html are used. We also use measurements of the in situ magnetic field obtained by the Electric and Magnetic Field Instrument Suite and Integrated Science instrument (http://emfisis.physics.uiowa.edu/about/instrument) to compare with the model magnetic field [*Tsyganenko and Sitnov*, 2005] used in the analysis of the TWINS ENA images.

The Comprehensive Inner Magnetosphere -Ionosphere (CIMI) [*Fok et al.*, 2014] model solves for the particle distribution functions in the ring current and the radiation belt plasmas, along with the plasmasphere density, region 2 currents, and ionosphere potential. CIMI provides modeled 3-D spatial structures, energy, and pitch angle distributions of energetic ions and electrons. The ionosphere potential is calculated self-consistently with the magnetospheric particle pressure gradient [*Fok et al.*, 2001]. CIMI also follows how particles and energy in the inner magnetosphere are enhanced and lost through the appropriate physical processes. In this study, drift paths from the CIMI model are employed to illustrate how pitch angle-dependent drift may be responsible of the observed characteristics of the ion pressure anisotropy.

3. Observations

3.1. Pertinent Geomagnetic Activity Parameters

Figure 1 shows the *SYM-H* from the OMNI database during the main phase of the storm on 17 March 2015. Following a fairly strong sudden storm commencement between 05:00 and 06:00 UT, *SYM-H* falls rapidly until approximately 09:30 UT, where it rises to a local peak at about 12:00 UT. It then falls somewhat steadily until just after 17:00 UT. At this time TWINS1 is in good position to observe the storm for the next 6 h. This period, shown in yellow, is the focus of this study. Note that just after 17:00 UT there is a local minimum in *SYM-H* and a local peak for a little over an hour, before *SYM-H* falls to the storm minimum just before 23:00 UT when the recovery phase begins. Note that the minimum *SYM-H* is approximately −230 nT, making this a strong storm.

Figure 2 shows the *AE* index for the same day also from the OMNI database. Note the high values of *AE* between 13:00 and 15:00 UT. There is also significant activity during the last 6 h of the main phase, shown in yellow, which is the focus of this study. There are several peaks in *AE* with magnitudes between 1000 and 1500 nT. We will interpret the *AE* index as an indicator of injections and perhaps substorms.

3.2. Total Ion Flux as a Function of Time and Location

In order to illustrate the temporal and spatial variations in the trapped particle ring current during the last 6 h of this strong storm, ion energies from 5 to 65 keV in 5 keV steps have been analyzed. The 30 keV results are presented here as typical.
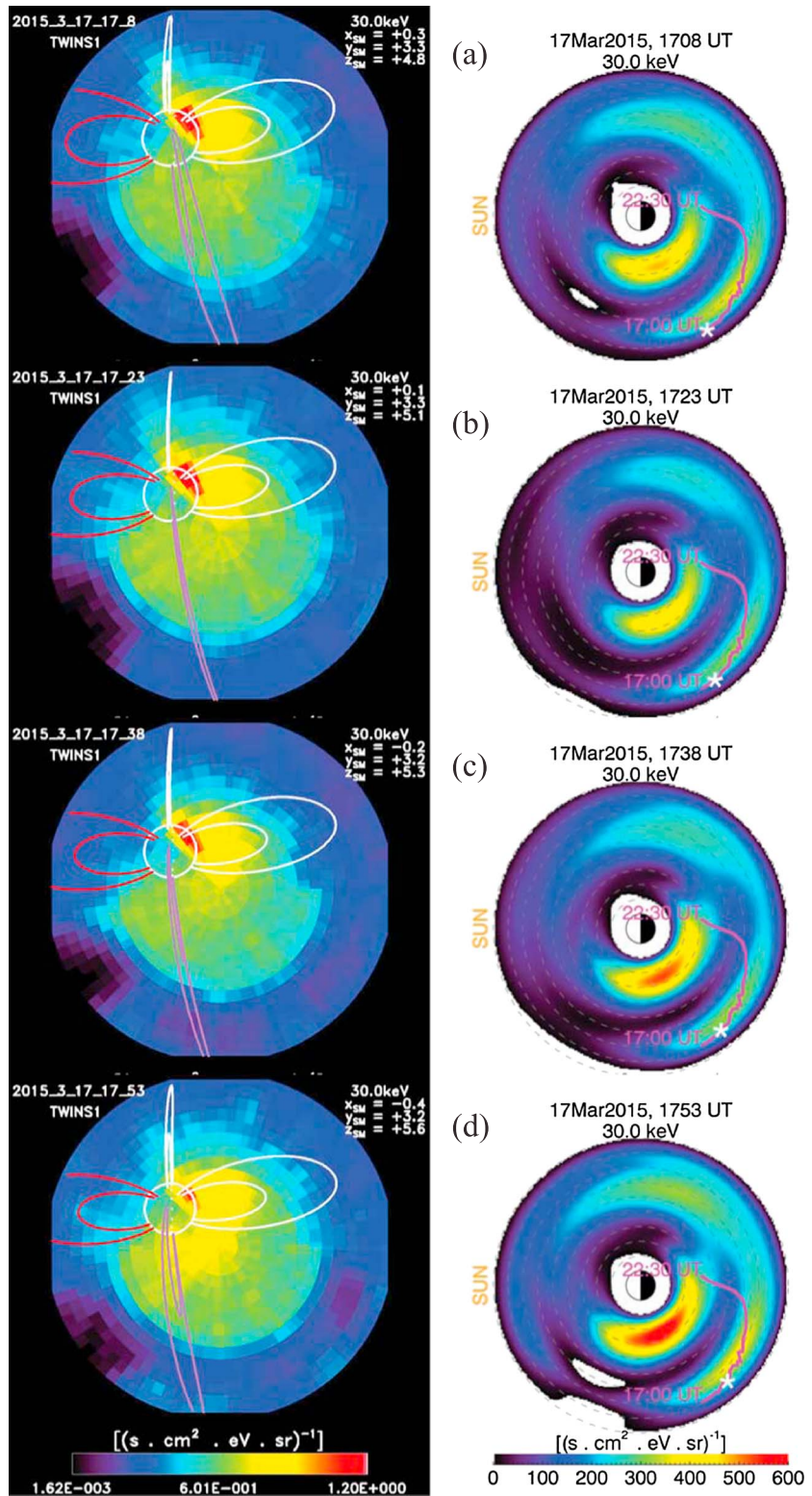
Figure 3. The 30 keV TWINS ENA images and deconvolved ion flux for 1 h on 17 March 2015. The images are integrated over approximately 15 min and over the energy range from 15 to 45 keV. (left) The ENA images are plotted on a log scale in a SkyMap format. Dipole field lines at $L = 4$ and 8 are drawn to guide the eye. The red lines point toward the Sun and the purple lines toward dusk. (right) The ion flux is plotted with a linear scale which is the same for all times. The central times are (a) 17:08, (b) 17:23, (c) 17:38, and (d) 17:53 UT.
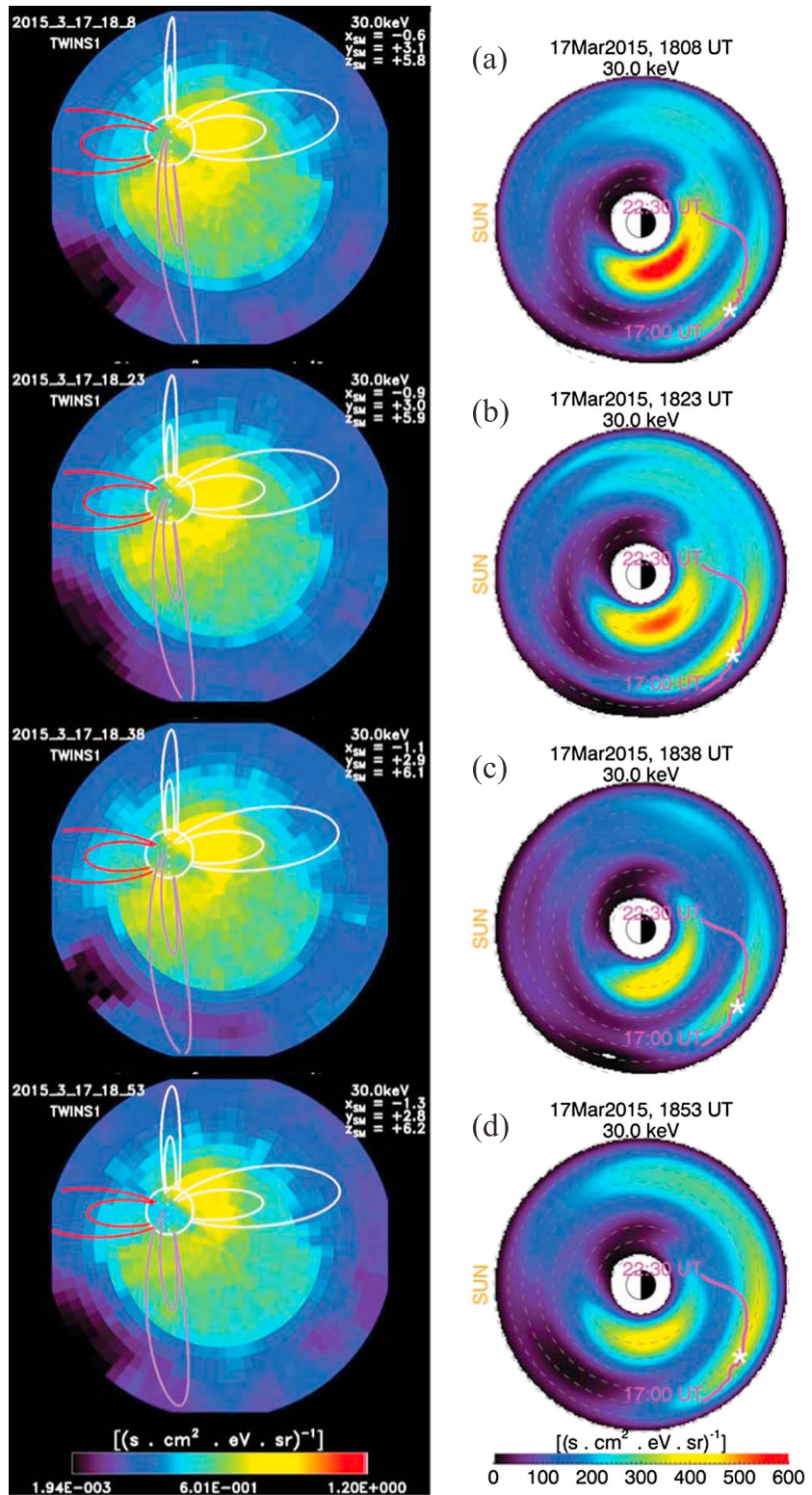
Figure 4. The 30 keV TWINS ENA images and deconvolved ion flux for 1 h on 17 March 2015 in the same format as in Figure 3. The central times are (a) 18:08, (b) 18:23, (c) 18:38, and (d) 18:53 UT.

Figure 5. The 30 keV TWINS ENA images and deconvolved ion flux for 1 h on 17 March 2015 in the same format as in Figure 3. The central times are (a) 19:07, (b) 19:23, (c) 19:37, and (d) 19:53 UT. Figure 5a shows the RBSPICE-A path from 16:59 to 22:29 UT.
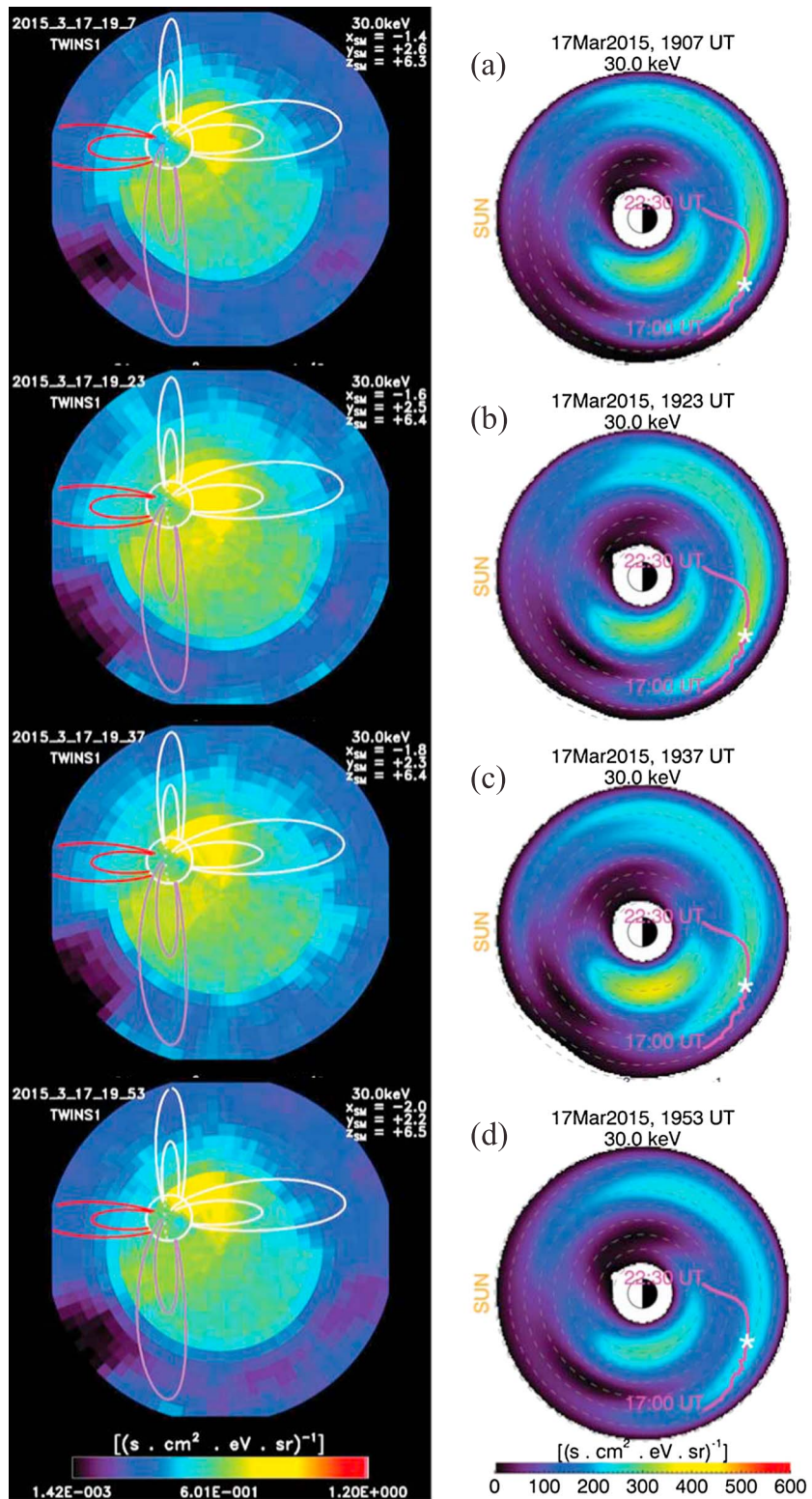
Figure 6. The 30 keV TWINS ENA images and deconvolved ion flux for 1 h on 17 March 2015 in the same format as in Figure 3. The central times are (a) 20:07, (b) 20:23, (c) 20:37, and (d) 20:53 UT.

Figure 7. The 30 keV TWINS ENA images and deconvolved ion flux for 1 h on 17 March 2015 in the same format as in Figure 3. The central times are (a) 21:07, (b) 21:23, (c) 21:37, and (d) 21:53 UT.
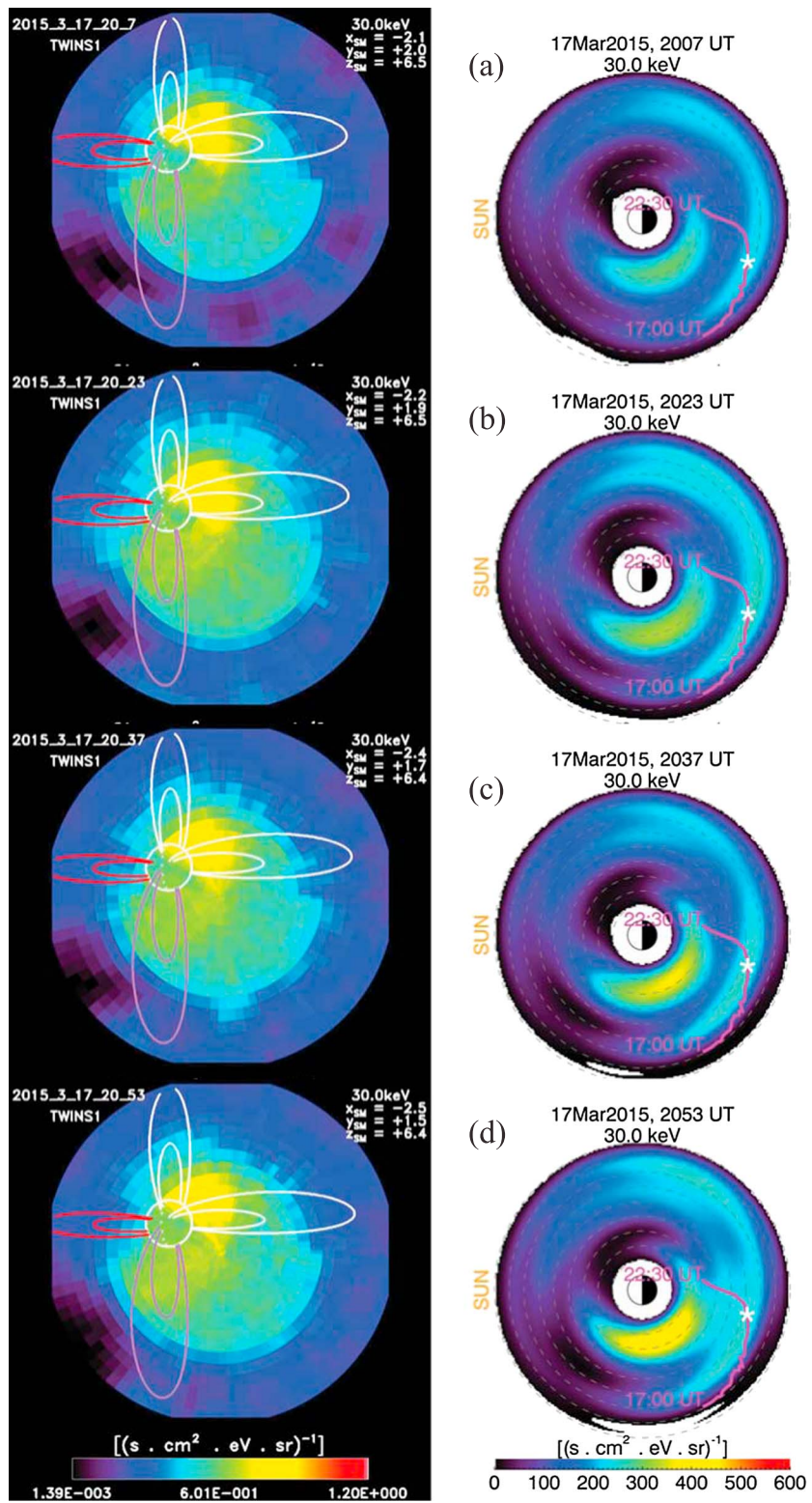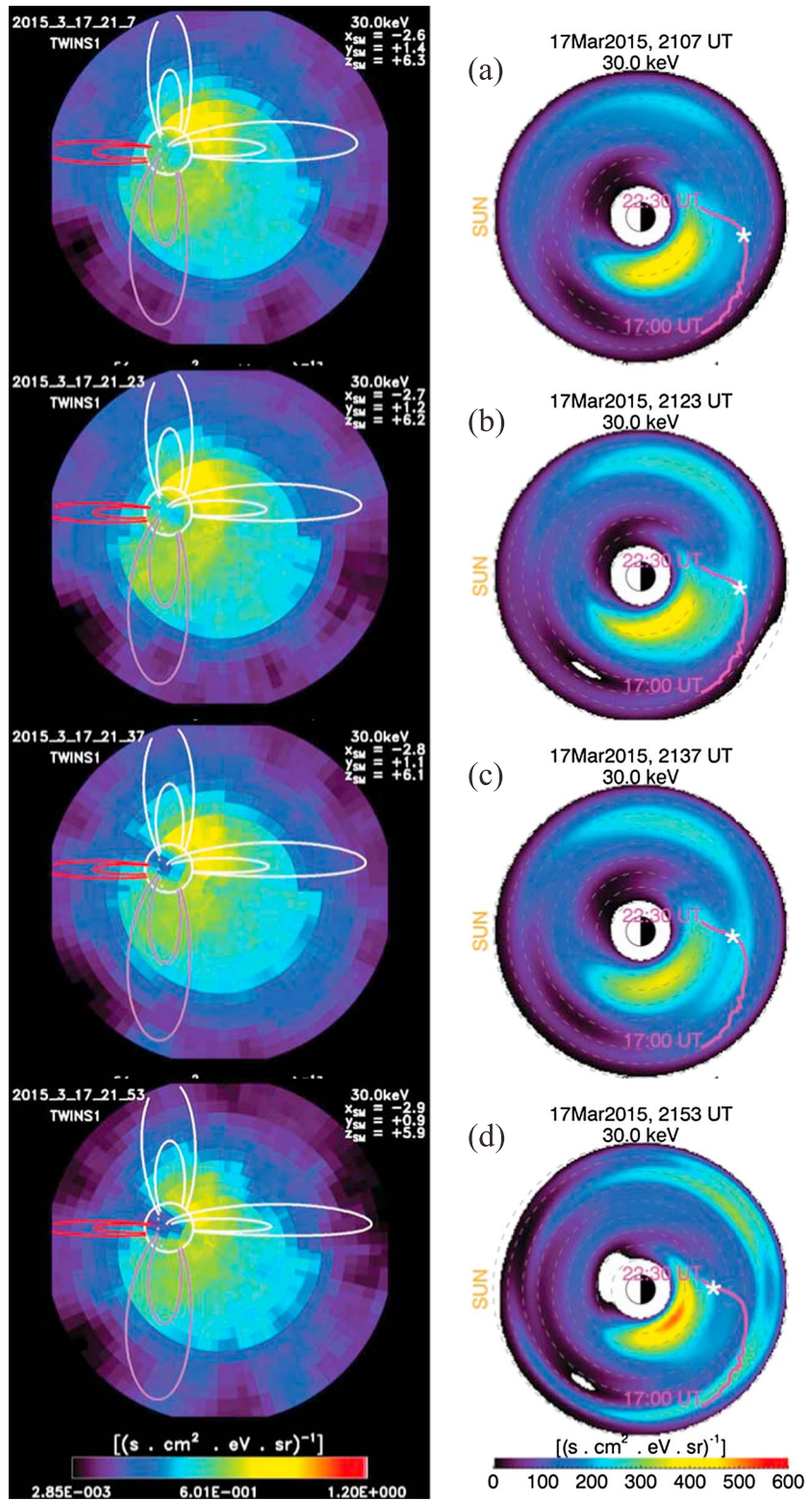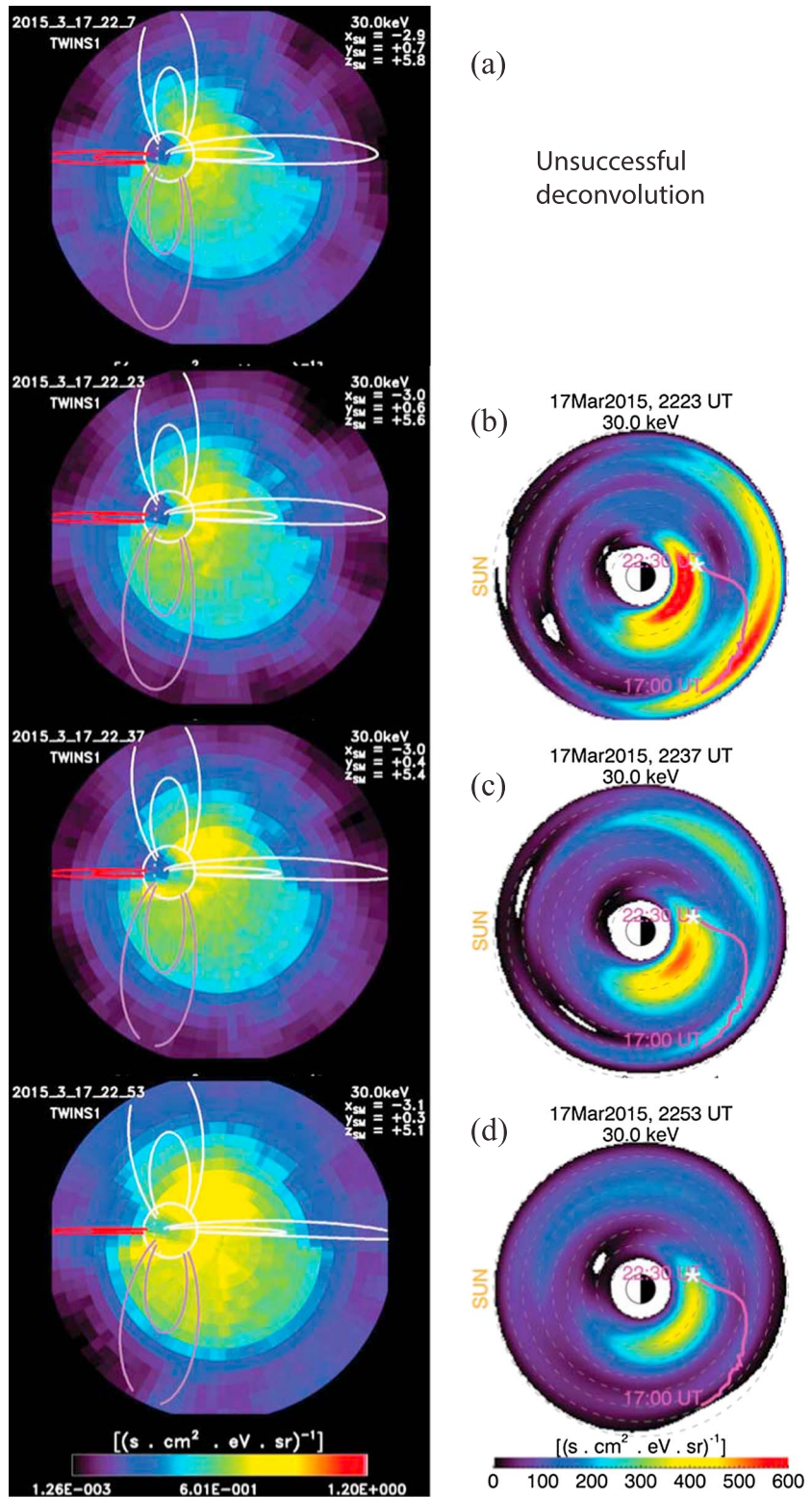
Figure 8. The 30 keV TWINS ENA images and deconvolved ion flux for 1 h on 17 March 2015 in the same format as in Figure 3. The central times are (a) unsuccessful deconvolution, (b) 22:23, (c) 22:37, and (d) 22:53 UT.
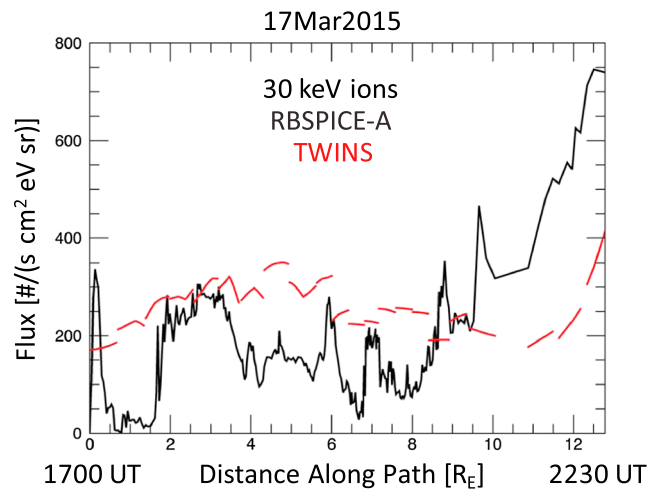
Figure 9. Comparison of 30 keV ion flux in situ measurements along the path of RBSPICE-A mapped to the SM equator and 15 min snapshots from the TWINS global images in Figures 3–8.

Figure 3 shows the first hour of 30 keV ion flux at 15 min intervals centered at 17:08, 17:23, 17:38, and 17:53 UT. Note the two strong peaks in the ion flux shown in the right column, one in the region of 3–4 R_E, 19:00–20:00 magnetic local time (MLT), and the other at 8–9 R_E, 21:00–23:00 MLT. The maximum flux in the inner peak rises during this hour, and the maximum of the outer peak remains lower relative to the inner peak. The ring current is clearly asymmetric during this time. It is to be noted that for the first 45 min, the ENA images in the left column show that the LAEs (bright red on the limb of the Earth) are the dominant emissions. The track of the RBSPICE-A satellite during the time period analyzed in this study is shown for each time interval mapped to the SM equator. The fact that the track is not perfectly smooth is indicative of the mapping in a disturbed magnetic field. The white star shows the mapped position of the satellite at the center time of each period.

Figure 4 shows the second hour of 30 keV ion flux at 15 min intervals centered at 18:08, 18:23, 18:38, and 18:53 UT. During this hour, the overall magnitude of the ion flux decreases. The inner peak remains the strongest. The strength of the outer peak fluctuates some. The ring current remains asymmetric. The ENA images show that the LAEs remain but are no longer the dominant emitters.

Figure 5 shows the third hour of 30 keV ion flux at 15 min intervals centered at 19:07, 19:23, 19:37, and 19:53 UT. During this hour, the overall magnitude of the ion flux declines compared to the previous hour with a small rise at 19:37 UT (Figure 8c). The inner peak remains in place. The outer peak fades during the last half hour. The ring current remains asymmetric, and the LAEs are present but not dominant. Figure 6 shows the fourth hour of 30 keV ion flux at 15 min intervals centered at 20:07, 20:23, 20:37, and 20:53 UT. The overall magnitude of the flux rises during the second half hour. The inner peak region remains in essentially the same location. The outer peak is still present but continues to fade. The ring current remains asymmetric, and the LAEs are present but not dominant.

Figure 7 shows the fifth hour of 30 keV ion flux at 15 min intervals centered at 21:07, 21:23, 21:37, and 21:53 UT. During this hour, the overall magnitude of the ion flux is steady during the first 45 min but increases in the last 15 min. The inner peak remains in the same location. The outer disappears and then returns but with a weak flux. The ring current remains asymmetric, and the LAEs are present but not dominant.

Figure 8 shows the sixth hour of 30 keV ion distributions at 15 min intervals. The deconvolution procedure was unsuccessful for the first 15 min interval because uncertainty estimates were not statistically valid, so there are results for periods centered at 22:23, 22:37, and 22:53 UT. The features of the trapped ring current particles change during this hour. At 22:23 UT, the inner peak moves into about 3 R_E and a little closer to midnight. The outer peak reappears briefly and is as bright as the inner peak. In the next half hour, the inner peak returns to a position similar to previous times. The outer peak once again fades and disappears. The overall magnitude is stronger at 22:23 UT but declines again in the last half hour. It is to be noted (see Figure 2) that the *AE* activity index has dropped precipitously during this hour. At 22:53 UT (Figure 8d), the outer peak has disappeared completely.

A direct comparison with the ion fluxes obtained from the ENA images and in situ measurements is difficult. Not only are the in situ measurements at a much higher cadence giving significantly higher resolution but the measurements along the satellite path apply to the entire series of global images because the ENA images give global snapshots of the entire inner magnetosphere over a period of time. Figure 9 shows the flux along the RBSPICE-A path mapped to the SM equator from 17:00 UT to 22:30 UT. At 16:59 UT, RBSPICE-A is well
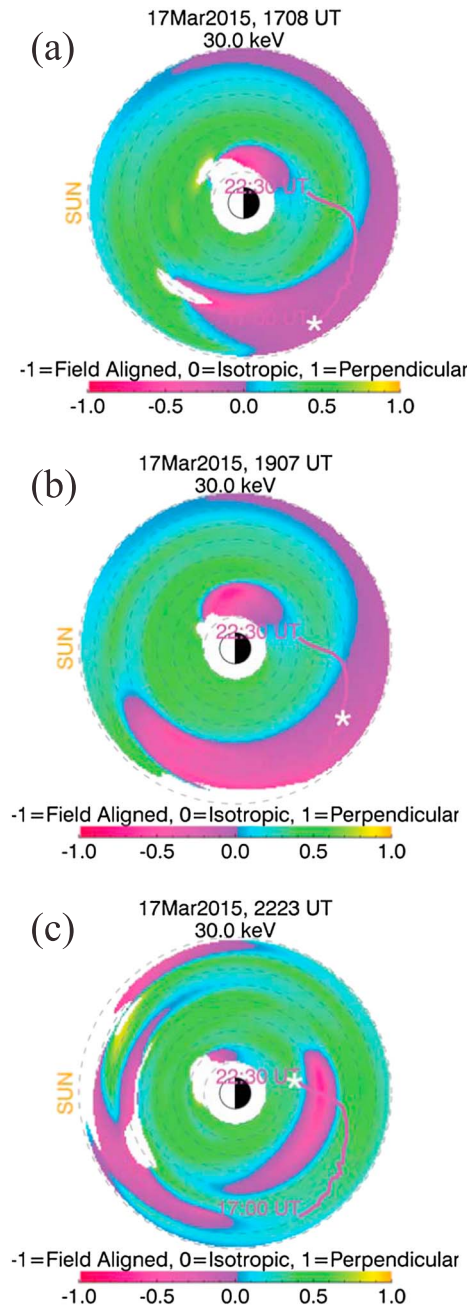
Figure 10. Pitch angle anisotropy for 30 keV ions extracted from the TWINS ENA images for 3 times spanning the 6 h focused upon in this study. The central times are (a) 17:08, (b) 19:07, and (c) 22:53 UT. Figure 10b shows the RBSPICE-A path from 16:59 to 22:29 UT. The color bar is chosen to emphasize the transition from perpendicular to parallel pitch angle anisotropy.

outside the inner peak in the TWINS results at about 22:00 MLT (see Figure 16a). It moves toward midnight where it crosses through the outer peak until it turns toward Earth and crosses midnight by 22:29 UT, where it passes at the edge of the inner peak in the TWINS results (see Figure 8d). It is not appropriate to compare the in situ observations with the flux in any single global image as the satellite is traveling through the region of the inner magnetosphere, where the flux is clearly time dependent. To minimize the mixing of location and time, what is shown in Figure 9 is a series of red lines representing the ion flux observed by TWINS at the appropriate location in each of the images shown in Figures 3–8. Note that the vertical axis is a linear scale. The significance of this comparison with regard to confidence in the ion fluxes obtained from the TWINS ENA images is discussed in section 5.

3.3. Ion Pressure Anisotropy

The ion flux extracted from the TWINS ENA images provides global images of the energy-dependent pitch angle anisotropy defined as [*Chen et al.*, 1998]

$$A = \frac{I_\perp - 2I_\parallel}{I_\perp + 2I_\parallel}$$

where

$$I_\perp \equiv \int_{-1}^{1} f_{eq} \sin^2 \alpha \; d(\cos \alpha) \quad \text{and}$$
$$I_\parallel \equiv \int_{-1}^{1} f_{eq} \cos^2 \alpha \; d(\cos \alpha)$$

and f_{eq} is the ion distribution as a function of energy at the SM equator and α is the pitch angle.

Figure 10 shows the 30 keV anisotropy for three times, 17:08, 19:07, and 22:23 UT, on 17 March 2015,

i.e., the last 6 h of the main phase of the storm. Note that inside of $L = 6$ in the dusk-to-midnight sector, the anisotropy is perpendicular, but it becomes slightly parallel outside of $L = 6$. Later in the 6 h period focused upon in this study, when the outer peak fades, the region of parallel pitch angles shrinks (see Figure 10c).

Integrating over energy gives the perpendicular and parallel pressure as a function of time and location. Figure 11 shows a comparison between the RBSPICE-A and the TWINS results. In this plot instead of mapping the RBSPICE-A results to the SM equator, the location of the TWINS flux, the TWINS flux is mapped to the RBSPICE-A location. This is because of difficulty in mapping the RBSPICE-A pitch angles, which are highly variable
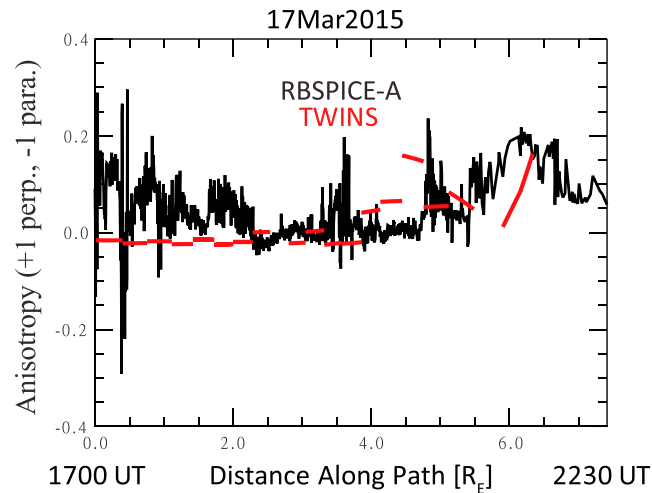
Figure 11. Comparison of ion pressure anisotropy in situ measurements along the path of RBSPICE-A shown in Figure 10b and 15 min snapshots obtained from the TWINS global ENA images.

in some cases and have missing data at approximately 5–10% of the pitch angles. Otherwise the format of this plot is the same as in Figure 9, i.e., 15 min snapshots of the TWINS results at the appropriate locations. The gaps in the TWINS anisotropies at the end of the track are due to difficulty in obtaining pitch angles at all energies. Note that the RBSPICE-A results show a high variability in the anisotropy, especially in the first 2 R_E of the path where the TWINS anisotropy is slightly parallel. The TWINS results miss the rise to perpendicular anisotropy in the RBSPSICE-A results at approximately 3.5 R_E along the path but show rises that are located approximately 0.5 R_E from where they are observed by RBSPICE-A in the final few Earth radii. The significance of this comparison with regard to confidence in the ion fluxes obtained from the TWINS ENA images is discussed in section 5.

4. Discussion

4.1. Total Ion Flux as a Function of Time and Location

The multiple-peak structure observed during the main phase of this storm is similar to that found in earlier, weaker storms on 29 May 2010 (minimum *SYM-H* = −70 nT, at the beginning of the recovery phase) and 26 May 2011 (minimum *SYM-H* = −30 nT, early in the main phase) [*Perez et al.*, 2015]. In this study of a very strong storm, we are able to follow the multiple peaks in the spatial structure for a full 6 h. We see that the inner peak is relatively stationary until very near the end of the main phase. This is a typical feature of ion distributions obtained from ENA images during the main phase [*Mitchell et al.*, 2001; *Pollock et al.*, 2003; *Perez et al.*, 2004b]. The outer peak, however, shows considerable variability in strength and then disappears in the last hour. It is tempting to associate the rise and fall of the outer peak with the extensive *AE* activity that could be associated with injections from the tail prior to and during this time period (see Figure 2). But substorms have been observed to be accompanied by more than one
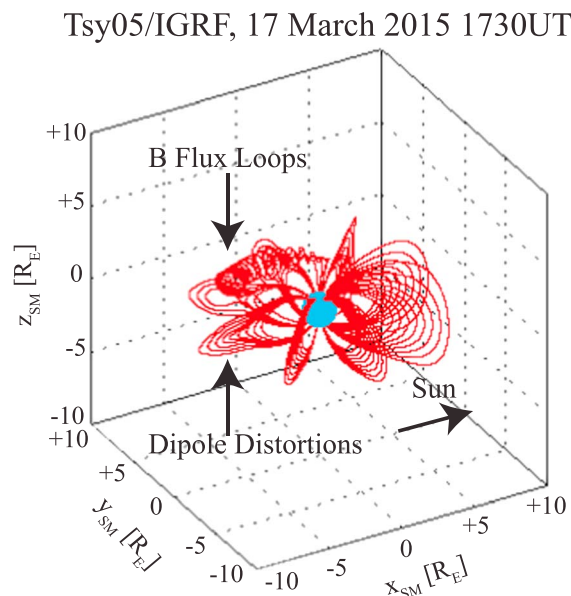

Figure 12. The 3-D plot of Tsy05 magnetic field at 17:30 UT on 17 March 2015 showing highly disturbed, i.e., nondipolar, fields.

$$\mu = 9.3 \times 10^6 \text{ keV/T}$$
$$\alpha = 4.7°$$

$$\mu = 1.3 \times 10^9 \text{ keV/T}$$
$$\alpha = 72°$$
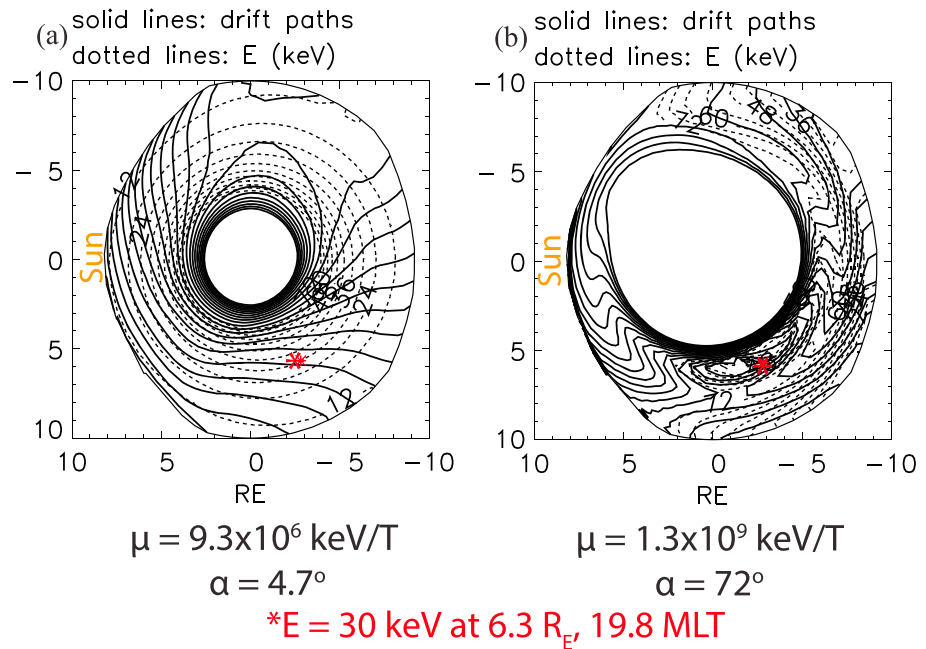
*E = 30 keV at 6.3 R_E, 19.8 MLT

Figure 13. Typical energy-dependent drift paths in the Tsyganenko magnetic field model during the last 6 h of the main phase of the storm on 17 March 2015. (a) Small first adiabatic invariant, μ, i.e., parallel pitch angles, α, and (b) large adiabatic invariant, μ, i.e., perpendicular pitch angles, α. The red stars mark the positions of a 30 keV ion at 6.3 R_E, 19:08 MLT.

injection [*Gkioulidou et al.*, 2015], and there can also be injections that do not result in auroral activity [*Russell et al.*, 2000]. Definitive understanding of this phenomenon would benefit from self-consistent simulations of the tail and inner magnetosphere.

Other features of the spatial and temporal distributions of the TWINS results are also consistent with the previous ENA observations. The fact that the ring current is asymmetric in the main phase of a strong storm is consistent with earlier results [*Pollock et al.*, 2001; *Brandt et al.*, 2001] from the Imager for Magnetopause-to-Aurora Global Exploration (IMAGE) satellite [*Burch*, 2000]. The fact that the LAEs are dominant in the earlier part of the main phase is consistent with results from *Valek et al.* [2010].

It can be noted that the disappearance of the outer ion peak at 30 keV at the end of the main phase is coincident with a very steep descent in *SYM-H* and a sharp drop in *AE* for over an hour. The relationship between the energy in the trapped particles in the ring current and *SYM-H* will be the subject of a future investigation.

4.2. Ion Pressure Anisotropy

To address the pitch angle variability shown in both the TWINS ion flux and the RBSPICE-A observations, Figure 12 shows a 3-D plot of the magnetic field at 17:30 UT from the Tsy05 [*Tsyganenko and Sitnov*, 2005] magnetic field model. The severe distortions from a magnetic dipole field at midnight and the flux rope at *L* values greater than 4 just after dusk suggest that the pitch angle anisotropy presented in section 3 could be a result of pitch angle-dependent drift very different from that expected in a dipole magnetic field.

This point is illustrated in Figures 13a and 13b, which show Hamiltonian contours (drift paths) for particles with constant first and second adiabatic invariants, i.e., μ and K, calculated from CIMI [*Fok et al.*, 2014] in the Tsy05 model magnetic field during the main phase of the 17 March 2015 storm. The solid lines in both plots are the drift paths for particles with constant first adiabatic invariant, i.e., μ. In Figure 13a, μ is the small representing ion with parallel pitch angles. In Figure 13b, μ is the large representing ion with perpendicular pitch angles. The dashed lines are the constant ion energy contours. In the simulations, as ions drift in from the plasma sheet to the ring current region, their first and second adiabatic invariants are conserved, but energy is changing. The locations of the ions which have energy of 30 keV at 6.3 R_E, 19:08 MLT, are marked with red asterisks in both Figures 13a and 13b. As shown in Figure 12, during the storm main phase of the ring current, the magnetic field is highly asymmetric. This produces a highly disturbed field in the dusk-to-midnight sector resulting in a magnetic field, which is opposite to the geomagnetic field in the dusk-midnight
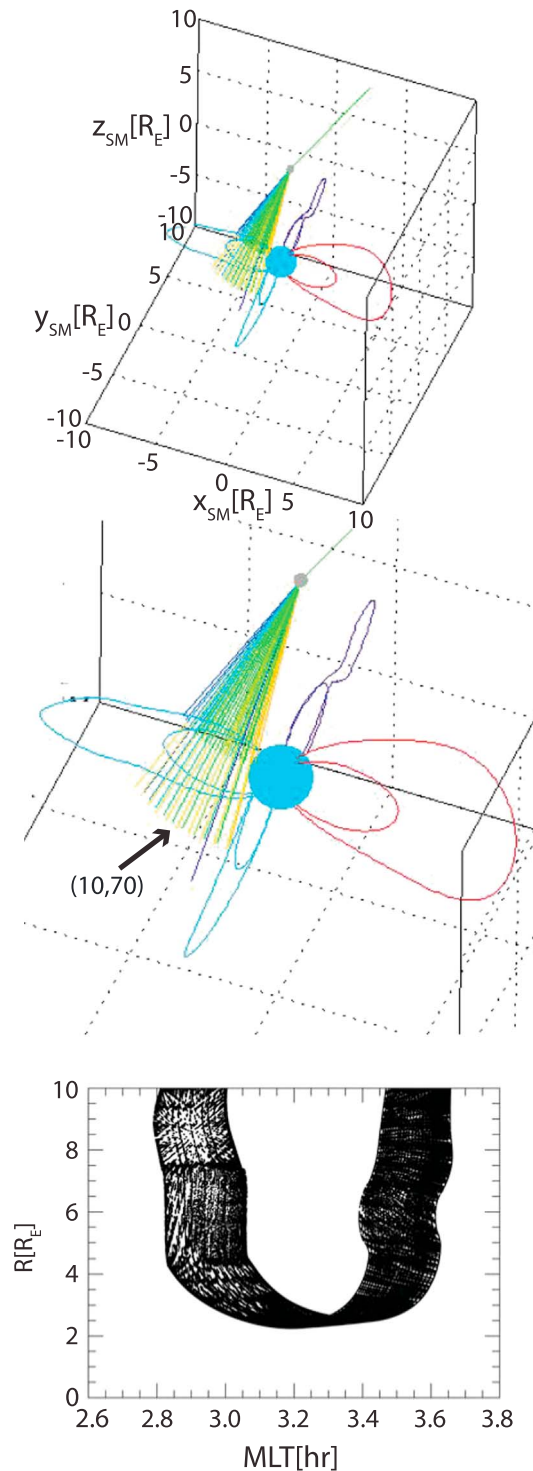
Figure 14. Illustrations showing how ENA pixels sample a range of radii and MLT values. (a) A 3-D view showing location of satellite and an array of pixels along with magnetic field lines from Tsy05 model. (b) Enlarged view of Figure 14a showing more detail and highlighting a specific pixel. (c) The range of radii (vertical axis) and MLT values (horizontal axis) that contribute to the pixel highlighted in Figure 14b.

sector. As a result, a local minimum in the magnitude of B is created. For field-aligned ions (Figure 13a), their magnetic drift is relatively weaker, so their drifts are dominated by convection and corotation. They drift across the low B region from nightside to dayside. Thus, ions with parallel pitch angles have access to the $L = 6$ region marked by the red star. In contrast, the magnetic drift of perpendicular ions follows the iso-contours of B and thus has closed drift paths in the minimum B region. Figure 13b shows that 30 keV ions with perpendicular pitch angles from the plasma sheet do not have access to the $L = 6$ region marked by the red star. It is the minimum in B and thus the closed B contours that are the determining factors. Plots for ions with other energies would have different values of μ but give very similar results and are not shown. This illustrates how the anisotropy in the region of the outer flux peak (see Figure 10) could be anisotropic in the parallel direction. The perpendicular anisotropy at the inner peak is what is expected from ions that have been injected into a region of higher magnetic field while conserving μ.

It is to be noted that the contours shown in Figure 13b do not imply that 30 keV ions do not have access to the inner magnetosphere. The plots are for constant μ. The 30 keV ions that do have access to the inner magnetosphere would have smaller values of μ.

5. Confidence in the Spatial Variations of the Flux Obtained From the ENA Images

In this section, we address the question of confidence in the double-peak structures in the trapped particle ring current that are observed by deconvolving ion flux from ENA images. First, it is to be noted that the methodology

employed provides a unique solution based upon Bayesian statistics and the assumption of no prior knowledge [*Wahba*, 1990]. The proscribed penalty function minimizes spatial variations in the sense of minimizing the second derivatives that are consistent with fitting the data in the sense of unit-normalized chi-square.

Multiple peaks in the trapped ring current ion spatial distribution obtained from ENA images have not been a regularly recurring feature. There have been a number of studies in which ion distributions have been extracted from ENA images. Beginning with results from the IMAGE [*Burch*, 2000] satellite, *Perez et al.* [2001], *Brandt et al* [2002a, 2000b, 2000c], *DeMajistre et al.* [2004], *Perez et al.* [2004b], *Vallat et al.* [2004], and *Zhang et al.* [2005] presented ion fluxes with single peaks. *Perez et al.* [2004a], however, did show spatial structures with indications of more than a single peak. For TWINS, *Grimes et al.* [2010], *Perez et al.* [2012], and *Grimes et al.* [2013] found similar hints of double peaks. *Perez et al.* [2015] show clear double peaks for brief times in two storms. So while the double peaks in the spatial dependence of the trapped ring current ion flux are not unprecedented, this feature does not seem to be an artifact of extracting ion distributions from ENA images.

It is to be noted that the double peaks in the ion flux are not apparent in the ENA images. This is explained by the fact that since we are imaging an "optically" thin magnetosphere, each pixel contains information from a range of radial and MLT values. This is illustrated in Figure 14. A 3-D global view is shown in Figure 14a. The Earth is at the center, and the region extending from -10 to $+10$ R_E is shown. The satellite is the grey spot above the Earth near dusk. Magnetic field lines at noon (red), dusk (purple), midnight (blue), and dawn (blue) at 4 and 8 R_E are shown. The volumes of a set of pixels from latitude 40° and longitude from 60° to 80° in satellite coordinates are shown by the green lines. Figure 14b shows a blown up version from the same perspective. Here it can be seen clearly that each pixel has contributions from a range of radial values at the equator. Focusing on the central pixel in this array denoted by the arrow in Figure 14b as an example, Figure 14c shows the equatorial radius and MLT values of the 874,058 points that contribute to ENAs in that pixel during the deconvolution process that results in the ion distributions.

There have been previous comparisons between the ion flux obtained from ENA images and in situ measurements. The first was *Vallat et al.* [2004], in which results from IMAGE-HENA were compared to "data provided by the Cluster Ion Spectrometry instruments on board the Cluster spacecraft." Statistical analysis [*Vallat et al.*, 2004, Figure 8] showed examples of reasonable agreement at high fluxes when plotted on a log scale. They also discussed the difficulty in estimating error bars for the ion distributions due to uncertainties in the magnetic field and geocorona density models necessary to obtain ions from the ENA images. *Grimes et al.* [2013] compared ion flux obtained from TWINS ENA images with in situ measurements by Time History of Events and Macroscale Interactions during Substorms (THEMIS) [*Angelopoulos*, 2008]. The time-dependent trends showed a good match, but the TWINS results were about a factor of 3 below the in situ measurements [*Grimes et al.*, 2013, Figure 6]. These examples illustrate not only the difficulty in reliably extracting ion distributions from ENA images but more importantly the fact that the two measurements reflect contrasting views. The in situ measurements give high time and space resolution at a series of points, while the ENA images present a global view averaged over both space and time. For example, the largest discrepancy between the TWINS fluxes and the in situ measurements from RBSPICE shown in Figure 9 is near the end of the track. If the ion flux peaks in the TWINS global image (Figure 8b) were moved slightly, the agreement would be much improved. Taken in context, the comparison of the TWINS fluxes with the in situ measurements from RBSPICE is excellent and provides confidence in the results from this study.

Both the in situ determination and extraction from ENA images of the pressure anisotropy are more challenging. *Grimes et al.* [2013] compared energy-dependent pitch angle anisotropies from TWINS ENA images with THEMIS in situ observations and found good agreement but it was during times when the pitch angle distributions were nearly isotropic. The pressure anisotropies from TWINS and RBSPICE-A shown in Figure 11 are much more dynamic. For the first 2 R_E of the RBSPICE path, the in situ measurements show a great deal of variability, including significant swings of parallel and perpendicular anisotropies, while the TWINS results are slightly parallel. It is clear that the TWINS ENA images cannot track the rapid variability of the in situ measurements. In the final 2 R_E of the path, the two plots show similar features including a peak of large perpendicular anisotropy at approximately 5 R_E along the path and a swing toward high perpendicular anisotropy at about 6 R_E. In both cases, the locations do not match exactly. It was pointed out in section 4.2 that a small change in the location of the flux peak in the TWINS flux would significantly improve the agreement. In light
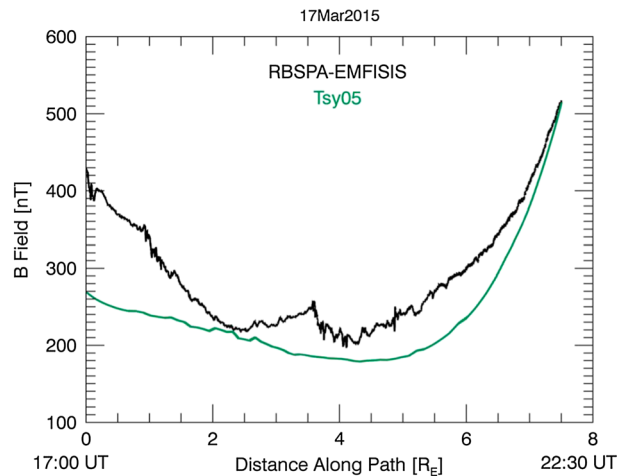
Figure 15. Comparison of Tsy05 magnetic model field with in situ measurements of RBSP A-EMFISIS.

of the fact that there is a different mix in space and time for the two measurements, the comparison supports confidence in the results of this study.

An important factor in the extraction of the ion fluxes as a function of position, time, pitch angle, and energy is the use of a model magnetic field. The Tsy05 model [*Tsyganenko and Sitnov*, 2005] is a data-based statistical model and is not expected to match perfectly event-specific in situ measurements especially in the case of the very strong storm being studied in this investigation. Figure 15 shows a comparison of the magnitude of the Tsy05 magnetic model field and the in situ field measured onboard RBSPICE-A. The trends are similar even though the agreement along the early part of the path is not as good as later in the path. We have already seen in the comparisons of the ion fluxes and pressure anisotropies that small changes in the spatial location of features in the TWINS fluxes would enhance the agreement with the in situ observations. It is reasonable, therefore, to conclude that the results of this study are not invalidated by the use of a statistical model for the magnetic field.

6. Summary and Conclusions

Ion flux and pressure anisotropy obtained from TWINS ENA images are shown for a 6 h period at the end of the main phase of a large storm (minimum $SYM\text{-}H = -230$ nT). The ion flux shows two peaks, an inner one at approximately radii = 3–4 R_E in the dusk-to-midnight sector and an outer peak at radii = 8–9 R_E prior to midnight. The position of inner peak is relatively stationary during the entire period. The flux that shows significant variations is magnitude. The outer peak shows the significant temporal variation brightening and dimming and finally disappearing at the end of the main phase. The pressure anisotropy shows the expected perpendicular pitch angles inside of 6 R_E but shows parallel pitch angles at larger distances. This is interpreted as consistent with pitch angle-dependent drift as modeled in the Tsy05 magnetic field and CIMI simulations.

The TWINS results are compared directly with RBSPICE-A measurements. Using 15 min snapshots of flux and pressure anisotropy from TWINS along the path of RBSPICE-A during the 6 h focused upon in this study, the essential features displayed in the TWINS global images are supported.

References

Angelopoulos, V. (2008), The THEMIS mission, *Space Sci. Rev.*, 141(1–4), 5–34, doi:10.1007/s11214-008-9336-1.

Bazell, D., E. C. Roelof, T. Sotirelis, P. C. Brandt, H. Nair, P. Valek, J. Goldstein, and D. McComas (2010), Comparison of TWINS images of low-altitude emission of energetic neutral atoms with DMSP precipitating ion fluxes, *J. Geophys. Res.*, 115, A10204, doi:10.1029/2010JA015644.

Brandt, P. C.:s., D. G. Mitchell, E. C. Roelof, and J. L. Burch (2001), Bastille Day storm: Global response of the terrestrial ring current, *Solar Phys.*, 204, 377–386, doi:10.1023/A:1014286728053.

Brandt, P. C.:s., S. Ohtani, D. G. Mitchell, R. Demajistre, and E. C. Roelof (2002a), ENA observations of a global substorm growth phase dropout in the nightside magnetosphere, *Geophys. Res. Lett*, 29(20), 1962, doi:10.1029/2002GL015057.

Brandt, P. C.:s., S. Ohtani, D. G. Mitchell, M.-C. Fok, E. C. Roelof, and R. Demajistre (2002b), Global ENA observations of the storm mainphase ring current: Implications for skewed electric fields in the inner magnetosphere, *Geophys. Res. Lett.*, 29(20), 1954, doi:10.1029/2002GL015160.

Brandt, P. C.:s., R. Demajistre, E. C. Roelof, S. Ohtani, D. G. Mitchell, and S. Mende (2002c), IMAGE/high-energy energetic neutral atom: Global energetic neutral atom imaging of the plasma sheet and ring current during substorms, *J. Geophys. Res.*, 107(A12), 1454, doi:10.1029/2002JA009307.

Burch, J. L. (2000), IMAGE mission overview, *Space Sci. Rev.*, 91, 1–14.

Chen, M. W., J. L. Roeder, J. F. Fennell, L. R. Lyons, and M. Schulz (1998), Simulations of ring current proton pitch angle distributions, *J. Geophys. Res.*, 103, 165–178, doi:10.1029/97JA02633.

deBoor, C. (1978), *A Practical Guide to Splines*, Springer, New York, doi:10.1007/978-1-4612-6333-3.

DeMajistre, R., E. C. Roelof, P. C.:s. Brandt, and D. G. Mitchell (2004), Retrieval of global magnetospheric ion distributions from high-energy neutral atom measurements made by the IMAGE/HENA instrument, *J. Geophys. Res.*, 109, A04214, doi:10.1029/2003JA010322.

Fok, M.-C., R. A. Wolf, R. W. Spiro, and T. E. Moore (2001), Comprehensive computational model of the Earth's ring current, *J. Geophys. Res.*, *106*, 8417–8424.

Fok, M.-C., N. Y. Buzulukova, S.-H. Chen, A. Glocer, T. Nagai, P. Valek, and J. D. Perez (2014), The Comprehensive Inner Magnetosphere-Ionosphere model, *J. Geophys. Res. Space Physics*, *119*, 7522–7540, doi:10.1002/2014JA020239.

Gkioulidou, M., et al. (2015), Spatial structure and temporal evolution of energetic particle injections in the inner magnetosphere during the 14 July 2013 substorm event, *J. Geophys. Res. Space Physics*, *120*, 1924–1938, doi:10.1002/2014JA020872.

Goldstein, J., and D. J. McComas (2013), Five years of stereo magnetospheric imaging by TWINS, *Space Sci. Rev.*, *180*, 39–70, doi:10.1007/s11214-013-0012-8.

Grimes, E. W., J. D. Perez, J. Goldstein, D. J. McComas, and P. Valek (2010), Global observations of ring current dynamics during corotating interaction region-driven geomagnetic storms in 2008, *J. Geophys. Res.*, *115*, A11207, doi:10.1029/2010JA015409.

Grimes, E. W., J. D. Perez, J. Goldstein, D. J. McComas, P. Valek, and D. Turner (2013), Comparison of TWINS and THEMIS observations of proton pitch angle distributions in the ring current during the 29 May 2010 geomagnetic storm, *J. Geophys. Res. Space Physics*, *118*, 4895–4905, doi:10.1002/jgra.50455.

Mauk, B. H., N. J. Fox, S. G. Kanekal, R. L. Kessel, D. G. Sibeck, and A. Ukhorskiy (2013), Science objectives and rationale for the Radiation Belt Storm Probes mission, *Space Sci. Rev.*, *179*, 3–27, doi:10.1007/s11214-012-9908-y.

McComas, D. J., H. O. Funsten, and E. E. Scime (1998), *Advances in Low Energy Neutral Atom Imaging, in Measurement Techniques in Space Plasmas: Fields*, Geophys. Monog. Ser., vol. 103, edited by R. F. Pfaff, J. E. Borovsky, and D. T. Young, pp. 275–280, AGU, Washington, D. C.

McComas, D. J., et al. (2009a), The Two Wide-angle Imaging Neutral-atom Spectrometers (TWINS) NASA mission-of-opportunity, *Space Sci. Rev.*, *142*(157), 231, doi:10.1007/s11214-008-9467-4.

McComas, D. J., et al. (2009b), Global observations of the interstellar interaction from the Interstellar Boundary Explorer (IBEX), *Science*, *326*, 959–962, doi:10.1126/science.1180906.

McComas, D. J., N. Buzulukova, M. G. Connors, M. A. Dayeh, J. Goldstein, H. O. Funsten, S. Fuselier, N. A. Schwadron, and P. Valek (2012), Two Wide-Angle Imaging Neutral-Atom Spectrometers and Interstellar Boundary Explorer energetic neutral atom imaging of the 5 April 2010 substorm, *J. Geophys. Res.*, *117*, A03225, doi:10.1029/2011JA017273.

Mitchell, D. G., K. C. Hsieh, C. C. Curtis, D. C. Hamilton, H. D. Voss, E. C. Roelof, and P. C.:s. Brandt (2001), Imaging two geomagnetic storms in energetic neutral atoms, *Geophys. Res. Lett.*, *28*, 1151–1154.

Mitchell, D. G., et al. (2013), Radiation Belt Storm Probes Ion Composition Experiment RBSPICE, *Space Sci. Rev.*, *179*, 263–308.

Perez, J. D., G. Kozlowski, P. C.:s. Brandt, D. G. Mitchell, J.-M. Jahn, C. J. Pollock, and X. X. Zhang (2001), Initial ion equatorial pitch angle distributions from medium and high energy neutral atom images obtained by IMAGE, *Geophys. Res. Letts.*, *28*, 1155–1158.

Perez, J. D., X.-X. Zhang, P. C.:s. Brandt, D. G. Mitchell, J.-M. Jahn, and C. J. Pollock (2004a), Dynamics of ring current ions as obtained from IMAGE HENA and MENA ENA images, *J. Geophys. Res.*, *109*, A05208, doi:10.1029/2003JA010164.

Perez, J. D., X.-X. Zhang, P. C.:s. Brandt, D. G. Mitchell, J.-M. Jahn, C. J. Pollock, and S. B. Mende (2004b), Trapped and precipitating protons in the inner magnetosphere as seen by IMAGE, *J. Geophys. Res.*, *109*, A09202, doi:10.1029/2004JA010421.

Perez, J. D., E. W. Grimes, J. Goldstein, D. J. McComas, P. Valek, and N. Billor (2012), Evolution of CIR storm on 22 July 2009, *J. Geophys. Res.*, *117*, A09221, doi:10.1029/2012JA017572.

Perez, J. D., J. Goldstein, D. J. McComas, P. Valek, N. Buzulukova, M.-C. Fok, and H. J. Singer (2015), TWINS stereoscopic imaging of multiple peaks in the ring current, *J. Geophys. Res. Space Physics*, *120*, 368–383, doi:10.1002/2014JA020662.

Pollock, C. J., et al. (2001), First medium energy neutral atom (MENA) images of Earth's magnetosphere during substorm and storm-time, *Geophys. Res. Letts.*, *28*, 1147–1150, doi:10.1029/2000GL012641.

Pollock, C. J., et al. (2003), The role and contributions of energetic neutral atom (ENA) imaging in magnetospheric substorm research, *Space Sci. Rev.*, *109*, 155–182.

Roelof, E. C. (1997), ENA emission from nearly-mirroring magnetospheric ions interacting with the exosphere, *Adv. Space Res.*, *20*, 361.

Russell, C. T., G. Lu, and J. G. Luhmann (2000), Lessons from the ring current injection during the September 24–25 1998 storm, *Geophys. Res. Letts.*, *27*, 1371–1374.

Spence, H. E., et al. (2013), Science goals and overview of the Radiation Belt Storm Probes (RBSP) Energetic Particle, Composition, and Thermal Plasma (ECT) suite on NASA's Van Allen Probes mission, *Space Sci. Rev.*, *179*, 311–336, doi:10.1007/s11214-013-0007-5.

Tsyganenko, N. A., and M. I. Sitnov (2005), Modeling the dynamics of the inner magnetosphere during strong geomagnetic storms, *J. Geophys. Res.*, *110*, A03208, doi:10.1029/2004JA010798.

Valek, P., P. C. Brandt, N. Buzulukova, M.-C. Fok, J. Goldstein, D. J. McComas, J. D. Perez, E. Roelof, and R. Skoug (2010), Evolution of low-altitude and ring current ENA emissions from a moderate magnetospheric storm: Continuous and simultaneous TWINS observations, *J. Geophys. Res.*, *115*, A11209, doi:10.1029/2010JA015429.

Vallat, C., et al. (2004), First comparisons of local ion measurements in the inner magnetosphere with energetic neutral atom magnetospheric image inversions: Cluster-CIS and IMAGE-HENA observations, *J. Geophys. Res.*, *109*, A04213, doi:10.1029/2003JA010224.

Wahba, G. (1990), *Spline Models for Observational Data*, Soc. for Ind. and Appl. Math., Philadelphia, Pa., doi:10.1137/1.9781611970128.

Zhang, X. X., J. D. Perez, T. Chen, C. Wang, P. C. Brandt, D. G. Mitchell, and Y. L. Wang (2005), Proton temperatures in the ring current from ENA images and in situ measurements, *Geophys. Res. Lett.*, *L16101*, doi:10.1029/2005GL023481.

Zoennchen, J. H., U. Nass, and H. J. Fahr (2015), Terrestrial exospheric hydrogen density distributions under solar minimum and solar maximum conditions observed by the TWINS stereo mission, *Ann. Geophys.*, *33*, 413.